Research Article

BIOMEDICAL Journal of Scientific & Technical Research

ISSN: 2574 -1241

DOI: 10.26717/BJSTR.2026.65.010157

Preparation and Electrochemical Properties of Western Medicine Slag-Based Capacitive Carbon

Zhang Xin[1]*, Kang Wei Wei[1,2], Yi Gui Yun[1] and Wang Jie[1]

[1]*School of Chemistry and Chemical Engineering, Henan Polytechnic University, Jiaozuo Henan 454003, China*

[2]*School of Physical Sciences, Qingdao University, Qingdao Shandong 266071, China*

***Corresponding author:** Zhang Xin, School of Chemistry and Chemical Engineering, Henan Polytechnic University, Jiaozuo Henan 454003, China

ARTICLE INFO

Received: March 16, 2026

Published: April 01, 2026

Citation: Zhang Xin, Kang Wei Wei, Yi Gui Yun and Wang Jie. Preparation and Electrochemical Properties of Western Medicine Slag-Based Capacitive Carbon. Biomed J Sci & Tech Res 65(2)-2026. BJSTR. MS.ID.010157.

ABSTRACT

To explore new pathways for the resource utilization of pharmaceutical solid waste, activated carbon was prepared using Western medicine residues as raw materials through a pre-carbonization–deashing–KOH activation process, and the effect of the alkali-to-carbon ratio on material structure and capacitance performance was systematically studied. The results show that with the increase of the alkali-to-carbon ratio, the crystallinity of the activated carbon decreased, defect concentration increased, specific surface area increased from 357.96 m2/g to 3131 m2/g, total pore volume increased from 0.325 cm3/g to 2.8 cm3/g, and micropore ratio reached a maximum of 39.89%. When the alkali-to-carbon ratio was 3:1, the resulting activated carbon exhibited a specific capacitance of 326 F/g at a current density of 0.5 A/g and maintained 245 F/g at 10 A/g, with a rate capability of 75.1%. The symmetric supercapacitor assembled from it showed a specific capacitance of 248.6 F/g at 0.5 A/g in 6 M KOH electrolyte and a capacitance retention of 96.01% after 10,000 cycles; in 1 mol/L Et4NBF4/PC organic electrolyte, the device achieved an energy density of 26.74 Wh/kg and a power density of 4988.5 W/kg. This process achieves the transformation of Western medicine residues into high-performance energy storage materials.

Keywords: Western Medicine Residue; Biomass; Solid Waste Resource Utilization; Supercapacitor; Electrode Material

(Graphical Abstract).

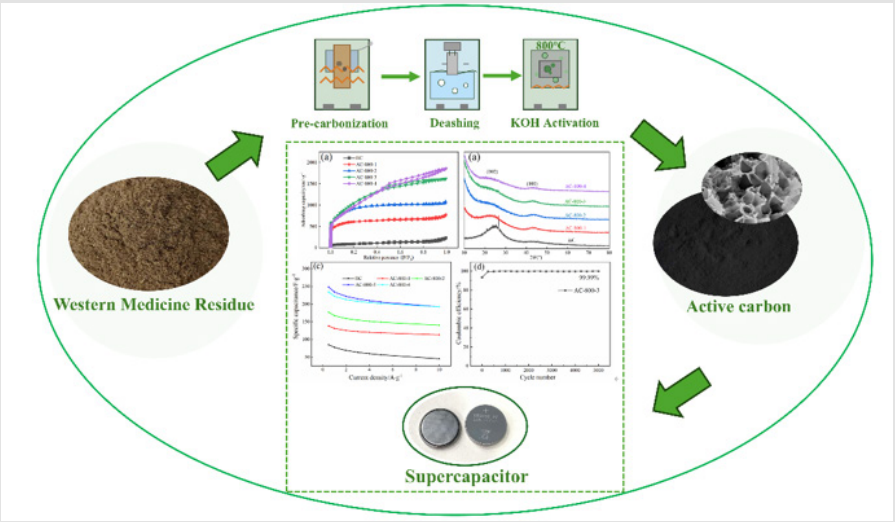

Abstract Figure

Introduction

With the improvement of health awareness, the continuous growth of people's demand for pharmaceutical products drives the rapid development of the pharmaceutical industry, and the prosperity of the pharmaceutical industry is also facing severe environmental challenges, the data shows that the annual output of pharmaceutical residue in the country has exceeded 10 million tons, of which 70 million tons of traditional Chinese medicine residue and about 1.9245 million tons of Western medicine residue. According to the "National Hazardous Waste List 2025 Edition", Western medicine residue is a hazardous waste and needs to be disposed of harmlessly through effective resource utilization. At present, conventional treatment methods for drug residue include landfill, incineration and open stacking. However, these methods have significant disadvantages: they can easily lead to groundwater and soil pollution, occupy a large amount of land resources, and are accompanied by potential environmental risks such as the release of heavy metal leachate and greenhouse gas emissions. The core of the harm of Western medicine residue lies in its residual active drug ingredients, especially antibiotics and hormones. Once these ingredients enter the environment, they can pollute water and soil, disrupt ecological balance, give rise to drug-resistant bacteria, and ultimately threaten human health and food safety through various channels.

Therefore, the development of drug residue resource utilization technology with both economic and environmental benefits has become a hot area of interdisciplinary research. The existing resource utilization methods of chemical residue mainly include soil ecological amendments, biofuels, feed additives, composting treatment, and anaerobic fermentation to prepare biogas. Although these methods have achieved the recycling of drug residues to a certain extent, they still have problems such as low treatment efficiency and easy to cause secondary pollution. The residue is rich in cellulose, lignin, crude protein, crude fat and a variety of trace elements, which provides a material basis for its high-value utilization, and the pyrolysis and conversion of it to prepare biochar can not only effectively overcome the shortcomings of long treatment cycle and low utilization rate of traditional methods, but also have good applicability to complex Chinese medicine residue and Western medicine residue. Supercapacitors are energy storage devices between traditional capacitors and chemical batteries, which store electrical energy through electric double-layer capacitors and pseudocapacitor mechanisms, and are considered one of the most promising energy storage systems due to their excellent power density, reliable cycle life, ultra-fast charging rate, and wide range of operating conditions.

At present, supercapacitors have formed large-scale applications in many fields such as transportation, electronic equipment, and power systems, and continue to expand emerging scenarios. The core of supercapacitors lies in electrode materials, which are mainly conductive polymers, metal oxides, and carbon-based materials. As the mainstream material of current supercapacitor electrodes, carbon-based materials can efficiently transport electrons and absorb a large amount of charge due to their high conductivity, large specific surface area and excellent chemical stability, and occupy a dominant position in supercapacitor applications. Common carbon-based materials include carbon nanotubes (CNTs), graphene, activated carbon (AC) and other new carbon materials. It is particularly noteworthy that activated carbon occupies more than 90% of the supercapacitor electrode material market share due to its extremely high specific surface area, adjustable pore structure, and low cost. The key to the preparation of activated carbon lies in the selection of precursors, and the main sources include polymers (synthetic polymers and natural polymers), minerals (coal, asphalt and oil) and biomass.

Among them, widely available and environmentally friendly renewable biomass and biomass waste have been widely recognized as highly potential carbon precursors due to their sustainability and structural characteristics, for example: Han, et al. [1] prepared activated carbon from herbaceous waste (specific surface area >2000 m^2/g), with a specific capacitance of 127 F/g (retention rate of 92% at 30 mA/cm^2); Du, et al. [2] developed nitrogen-doped porous carbon from celery, achieving 402 F/g in 1 M H_2SO_4 (1 A/g) with a 97% retention after ten thousand cycles; Nattapat [3] assembled symmetric capacitors using cashew shell-derived carbon, reaching an energy density of 2.43 Wh/kg (1002 W/kg) with 87% cycle stability (1.0 A/g, 10,000 cycles). Therefore, biomass-based precursors, due to their renewability, abundant natural heteroatom resources, and diverse structural features, have become the ideal choice for preparing high-performance activated carbon electrodes for supercapacitors.

In view of this, this study uses Western medicine residues as precursors to prepare activated carbon for supercapacitors through high-temperature carbonization, deashing treatment, and chemical activation, investigates the effects of the alkali-to-carbon ratio on the microstructure and morphology of the activated carbon, evaluates its electrochemical performance as supercapacitor electrode material, and studies the structure–property relationship between the microstructure and electrochemical performance of activated carbon derived from Western medicine residues. This study achieves the conversion of Western medicine residue waste into functional carbon materials, significantly reducing the environmental risks of solid waste while creating considerable economic added value, perfectly aligning with the concept of sustainable development. At the same time, it demonstrates that activated carbon derived from waste biomass has great application potential as a low-cost, high-performance electrode material. This work provides important experimental evidence and theoretical support for developing widely available, inexpensive, and high-performance biomass-derived carbon materials and has positive significance for promoting the development of green energy storage devices.

Experiment

Reagents and Instruments

Hydrochloric acid (35% wt), Yantai Shuangshuang Chemical Co., Ltd.; anhydrous ethanol (99.5%), Tianjin Comeo Chemical Reagent Co., Ltd.; deionized water, Jiaozuo Xinbailong Trading Co., Ltd.; aqueous electrolyte (6 mol/L KOH solution, homemade); PTFE emulsion (60%), Dongguan Kelude Innovation Technology Co., Ltd.; supercapacitor electrolyte (1 M Et_4NBF_4/PC), Dongguan Kelude Innovation Technology Co., Ltd. Tube furnace (SK-G06123K, Tianjin Zhonghuan Electric Furnace Co., Ltd.); vacuum drying oven (DZF-6020AB, Beijing Zhongxing Weiye Instrument Co., Ltd.); electronic analytical balance (BS-224S, Baijing Saiduosi Instrument Company); electrochemical workstation (CHI 760E, Shanghai Chenhua Instrument Company); button cell sealing machine (MSK-110, Shenzhen Kejing Zhida Technology Co., Ltd.); vacuum glove box (Super(1220/750), Shanghai Micro-Na Electromechanical Technology Co., Ltd.).

Preparation of Activated Carbon from Chemical Medicine Residues

Weigh 500 g of Western medicine residue, put it in a solid sample crusher (model XA-3) for 1 minute, and sift it with a 200-mesh sieve. 20 g of sieve was weighed in a tube furnace (SK-G06123K), heated to 600 ℃ for 2 h at a heating rate of 5 ℃/min under N_2 atmosphere, and the carbonized material (initial ash fraction was 42.76%) after natural cooling. Hydrochloric acid (35 wt.%) was used to demineralize the carbonized material. Weigh 15 g of carbonized material in a 1000 mL beaker, add 500 mL of dilute hydrochloric acid solution (the volume ratio of deionized water to hydrochloric acid is 3:1), stir in a water bath at 60 ℃ for 3 h, then wash and filter, collect and purify the activated carbon for drying, reduce the ash content from 42.76% to 8.6%, and label it as BC. Weigh 5 g BC, mix with KOH according to the alkali-carbon ratio of 1:1, 2:1, 3:1, 4:1, and grind for 10 minutes. Then put into a tubular furnace and activate at a heating rate of 5 ℃/min to 800 ℃ for 2 h in an N_2 atmosphere, and collect the activation material after natural cooling. The activation material was pickled and prepared with 500 mL of hydrochloric acid solution (the volume ratio of deionized water to hydrochloric acid was 3:1), then the activation material was added, heated in a water bath at 60 ℃ for 3 h, then filtered, and the filter cake was repeatedly washed with deionized water until the filtrate was neutral (pH≈7). The washed samples were placed in a blast drying oven and dried at 80 ℃ for 12 h. The resulting activated carbon was named AC-800-1, AC-800-2, AC-800-3 and AC-800-4, corresponding to alkali-carbon ratios of 1:1, 2:1, 3:1 and 4:1, respectively.

Material Characterization

The microstructure of the activated carbon materials was characterized using a scanning electron microscope (SEM, Merlin Compact). The crystal structure was analyzed using an X-ray diffractometer (XRD, SmartLab (9 kW)), with the testing conditions: Cu target Kα radiation (λ=0.15406 nm) as the radiation source, scanning range of 10°-80°, scanning rate of 10°/min, and scanning step of 0.02°. The pore structure parameters of the samples (specific surface area, pore volume, pore size distribution) were measured using an independent four-station micropore physical adsorption analyzer. The defect degree of the materials was evaluated using a high-resolution confocal laser Raman spectrometer (alpha300R) with a laser wavelength of 532 nm and a testing range of 400-4000 cm^{-1}.

Preparation of Supercapacitor Electrode Materials and Evaluation of Electrochemical Performance

Mix activated carbon, conductive carbon black (Super-P), and the binder polytetrafluoroethylene (PTFE) in a mass ratio of 8:1:1 in an agate mortar. Add a small amount of anhydrous ethanol and grind for 30 minutes until a uniform paste is formed. Press the paste into sheets and then cut into round electrodes with a diameter of 10 mm. Dry the electrode sheets in a vacuum oven at 80 ℃ for 12 hours, weigh them, and set aside (mass range: 2–4 mg).

Three-Electrode System Testing: A 6 M KOH solution was used as the electrolyte. Working electrode preparation: cut a piece of nickel foam measuring 1×3 cm^2, wrap the above circular electrode sheet, and press it into a sheet using an electric powder press at a pressure of 10 MPa. The counter electrode was a platinum foil (1×1 cm^2), and the reference electrode was a Hg/HgO electrode. Testing was conducted using a Shanghai Chenhua Electrochemical Workstation (CHI760E). Galvanostatic charge/discharge (GCD) was performed over a potential range of -1-0 V, with current densities of 0.5 A/g, 1 A/g, 2 A/g, 3 A/g, 4 A/g, 5 A/g, and 10 A/g. Cyclic voltammetry (CV) was performed over a potential range of -1-0 V, with scan rates of 5 mV/s, 10 mV/s, 20 mV/s, 50 mV/s, and 100 mV/s. Electrochemical impedance spectroscopy (EIS) measurements were conducted with an amplitude of 5 mV and a frequency range of 0.01-100 kHz.

Aqueous Two-Electrode System Testing

Assembling CR2032-type symmetric supercapacitors: Use 6 M KOH solution as the electrolyte, glass fiber (Whatman, GF/C) as the separator, and select two circular electrodes with similar mass as the positive and negative electrodes. Let the assembled cell stand for 10 hours to allow the electrolyte to fully infiltrate. Perform GCD, CV, and EIS tests using the Shanghai Chenhua CHI760E workstation (parameters are the same as those in the three-electrode system, with the potential range set to 0-1 V). Use the LANDBlue (LAND) testing system for long-cycle performance testing: carry out 10,000 GCD cycles at a current density of 1 A/g. Set CV and GCD potential ranges to 0-1 V, with other testing parameters kept consistent with the three-electrode system.

Organic Two-Electrode System Testing

Assemble CR2032-type symmetric supercapacitors in an ultra-high purity argon glove box (H_2O < 0.01 ppm, O_2 < 0.01 ppm), with the electrolyte being supercapacitor electrolyte (Et_4NBF_4/PC) and the separator being glass fiber (Whatman, GF/C). After assembly, use a hydraulic press (MSK-110) to encapsulate and mold the cells. After standing for 10 hours, electrochemical testing is carried out using a Shanghai Chenhua CHI760E workstation (with the potential range set to 0–2.5 V, and other test parameters the same as those in the three-electrode system). The specific capacitance of the symmetric capacitor is calculated from GCD data, as shown in equation (1):

$$c = \frac{2I\Delta t}{m\Delta V} \quad (1)$$

In the formula, I, Δt, ΔV, and m represent the discharge current (A), discharge time (s), voltage change (V), and mass (g) of the single electrode active material, respectively.

The specific capacitance of the three-electrode testing system is calculated using formula (2):

$$c = \frac{I\Delta t}{m\Delta V} \quad (2)$$

In the formula, I is the discharge current (A), Δt is the discharge time (s), ΔV is the potential change (V), and m is the mass of the active material (g). The formulas for energy density E (in Wh/kg) and power density P (in W/kg) are shown in equations (3) and (4):

$$E = \frac{C\Delta V^2}{8\times 3.6} \quad (3)$$

$$P = \frac{3600E}{\Delta t} \quad (4)$$

In the formula, C is the specific capacitance of the capacitor (F/g); I is the charge-discharge current (A); Δt is the discharge time (s); m is the mass of the active material of a single electrode (g); ΔV is the voltage window during the discharge process (V).

Results and Discussion

Study on the Fundamental Physicochemical Properties of Chemical Medicine Residues

Proximate Analysis and Cellulose Analysis of Chemical Medicine Residues: The Western medicine residue used in this study was obtained from Henan Tianfang Pharmaceutical Co., Ltd., and its proximate analysis and cellulose analysis are shown in Tables 1 & 2. The volatile matter content of the Western medicine residue is 60%, the fixed carbon content is 13%, the ash content is 17%, and the moisture content is 10%. The contents of cellulose, hemicellulose, and lignin are 8.1%, 3.9%, and 9.8%, respectively. The data in Table 2 were determined by high-performance liquid chromatography (HPLC) combined with the NREL method. The total mass proportion of cellulose, hemicellulose, and lignin in the Western medicine residue is 21.8%, which is much lower than the total proportion of organic components in typical dry biomass, indicating that the Western medicine residue contains a higher proportion of ash and a large amount of volatile matter. The results of the proximate analysis in Table 1 (ash content 17%, volatile matter content 60%) also confirm this.

Table 1: Proximate Analysis (Mass Fraction).

Sample	Moisture/%	Ash/%	Volatile Matter/%	Fixed Carbon/%
Chemical Medicine Residue	10	17	60	13

Table 2: Cellulose Analysis (Mass Fraction).

Sample	Cellulose/%	Hemicellulose/%	Lignin/%
Chemical Medicine Residue	8.1	3.9	9.8

Thermogravimetric Analysis of Chemical Medicine Residues: Thermogravimetric analysis (TGA) was used to study the thermal decomposition behavior of pharmaceutical residue (Figure 1). Analysis of the TG curve shows that the pyrolysis process of the pharmaceutical residue can be divided into three main stages: The first stage is from room temperature to 170 °C, attributed to the release of water; this stage is mainly accompanied by the volatilization of low-molecular-weight compounds and adsorbed water, resulting in a sample mass loss of about 7%. The second stage occurs between 200-600 °C, corresponding to the large-scale removal of volatiles; this stage is mainly dominated by the thermal decomposition of cellulose and hemicellulose, while high-molecular-weight compounds undergo bond cleavage, generating small-molecule volatile products. The maximum decomposition rate occurs at 310 °C (0.34 %/min), and the cumulative weight loss in this stage reaches 56%. The third stage is above 600 °C, belonging to the formation and stabilization of the carbon skeleton, mainly involving the slow decomposition of lignin and the rearrangement of aromatic structures.

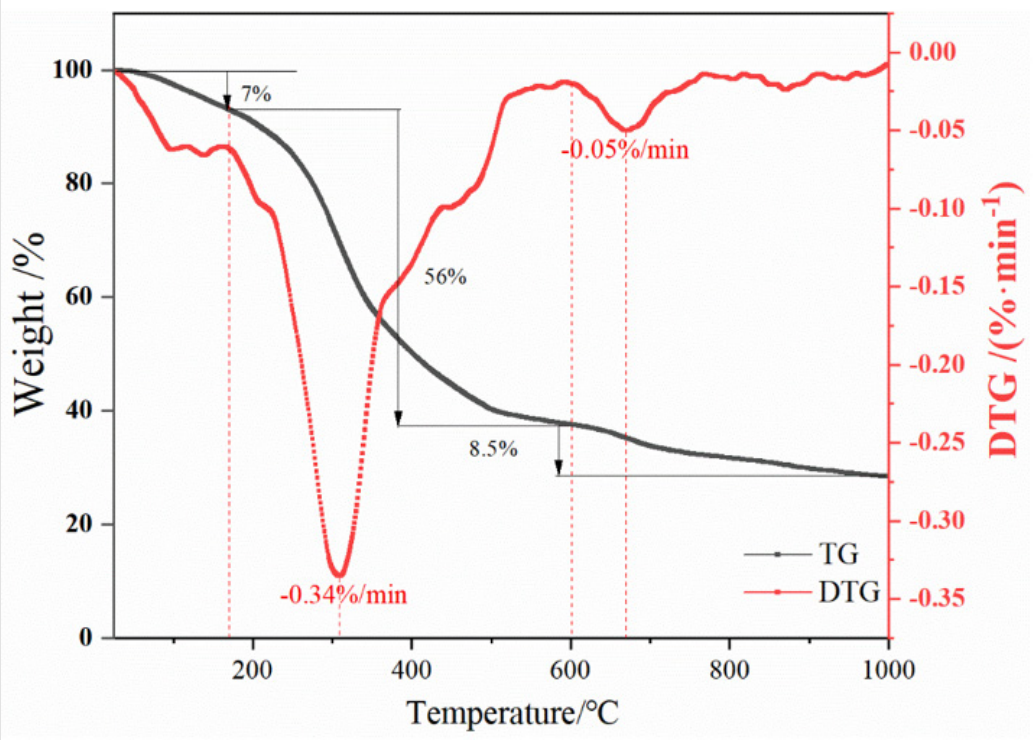

Figure 1: TG/DTG curve of Western medicine residue.

A decomposition rate peak appears at 670 ℃ (0.05 %/min), and as the temperature continues to rise, pyrolysis approaches completion and the carbonization process ends. In the carbonization process, too low a temperature easily causes incomplete removal of volatiles, affecting subsequent activation; too high a temperature will increase energy consumption. Therefore, reasonably selecting the carbonization temperature is crucial. Based on the above analysis, 600 ℃ is chosen as the carbonization temperature, which is more appropriate: at this temperature, the volatiles have been fully released, the carbon skeleton is initially formed, and energy consumption from high temperatures can be avoided.

Characterization of Activated Carbon Structure and Properties

X-ray Diffraction and Raman Spectroscopy Analysis: Figure 2(a) shows the XRD spectra of biochar (BC) and activated carbon samples (AC-800-1, AC-800-2, AC-800-3, and AC-800-4) activated with different alkali-carbon ratios. All samples had diffraction peaks at about 24° and 43°, and there were no other heterogeneous peaks, indicating that the resulting materials were all high-purity carbon materials. BC presents widened and weak diffraction peaks at the corresponding positions, which belong to the (002) crystal plane of graphite-like structure and the (100) crystal plane of amorphous carbon, respectively [4], indicating that BC is dominated by highly disordered amorphous carbon, with a low degree of crystallization and a small graphite crystalline size [5,6]. With the increase of the alkali-carbon ratio (from AC-800-1 to AC-800-4), the diffraction peak (002) gradually widens and shifts slightly to the lower angle, indicating that KOH activation significantly destroys the ordered structure of graphite microcrystals, resulting in a further decrease in material crystallinity, an increase in carbon layer spacing $d_{(002)}$, and a significant increase in defect density and pore structure [7].

The above analysis showed that increasing the alkali-carbon ratio could effectively promote the pore development and specific surface area of activated carbon, and reduce the degree of graphitization. The continuous widening of the diffraction peak further confirmed the decrease of crystal size and the increase of structural defects, indicating that the amorphous carbon characteristics of the material became more significant with the deepening of activation. The Raman spectra in Figure 2(b) show two distinct characteristic peaks near 1350 cm^{-1} and 1600 cm^{-1}, corresponding to the D-band for disordered structures or defects in carbon materials, and the G-band for oscillating within the lattice plane of sp^2 hybrid carbon atoms [8,9]. The D-band to G-band strength ratios (I_D/I_G) of BC, AC-800-1, AC-800-2, AC-800-3, and AC-800-4 were 0.89, 0.95, 1.01, 1.04, and 0.96, respectively, and the I_D/I_G values of activated activated carbon were higher than those of BC, and lower I_D/I_G values usually indicated a high degree of graphi-

tization [10], indicating that the activation of KOH reduced the degree of graphitization. It was shown that the activation process improved the porosity of the activated carbon structure and enhanced the disorder of the material, and more defects provided more adsorption sites for ion adsorption, while graphitized carbon with good conductivity also promoted charge transfer.

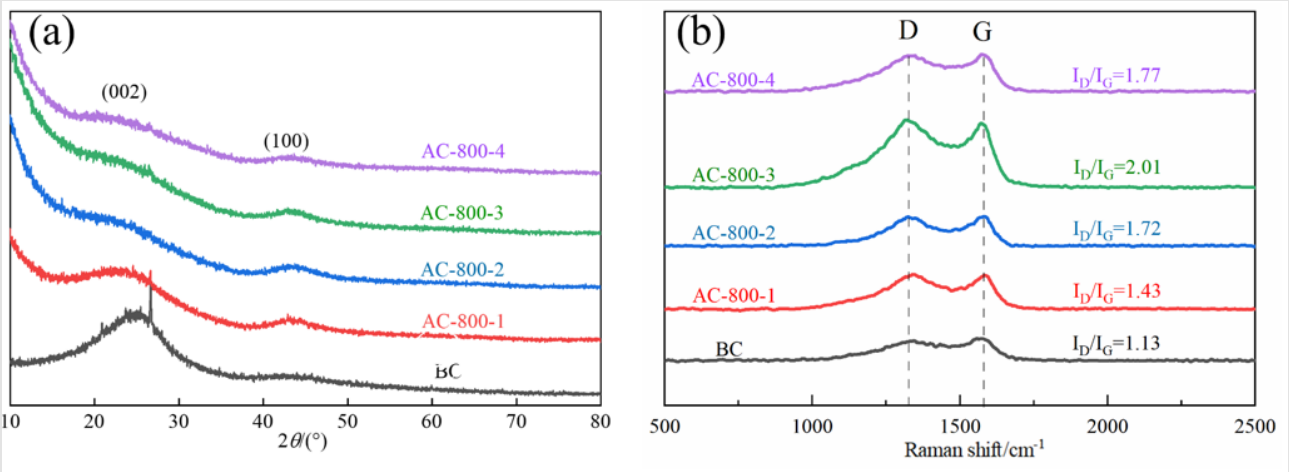

Figure 2:
a) XRD pattern and
b) Raman spectrum of activated carbon.

Adsorption Isotherms and Pore Structure Analysis: According to the classification criteria of the International Union of Pure and Applied Chemistry (IUPAC), the N_2 adsorption-desorption isotherms of BC, AC-800-1, and AC-800-2 exhibit typical I-type characteristics (Figure 3a), and their adsorption capacity increases rapidly in the lower relative pressure region ($P/P_0 < 0.01$), indicating that the sample is dominated by microporous structure [11], which is consistent with the higher microporosity in the pore size distribution (Figure 3b) and the corresponding pore structure parameters (Table 3). In contrast, the isotherms of AC-800-3 and AC-800-4 show the composite characteristics of type I and type IV: the adsorption capacity increases sharply at very low relative pressure, indicating the presence of significant micropores. In the medium-pressure region (0.4~0.95 P/P0), a significant lag ring appears, indicating capillary cohesion and revealing the existence of mesopores [12]. The adsorption capacity continued to rise when approaching saturated vapor pressure ($P/P_0 \approx 1$), suggesting that there were a small number of macropores in the material.

Table 3: Pore structure parameters of activated carbon.

Sample	S_{BET}/m^{2}–g-1	V_{total}/cm^3-g^{-1}	V_{micro}/cm^3-g^{-1}	$V_{micro}/V_{total}/\%$	Daverage/nm
BC	357.968	0.3254	0.116	35.6	5.185
AC-800-1	2017.58	1.201	0.575	47.88	3.31
AC-800-2	3388.825	2.176	1.21	55.6	2.568
AC-800-3	3525.199	2.74	1.207	44.05	3.109
AC-800-4	3131.602	2.8	1.117	39.89	3.577

 DOI: 10.26717/BJSTR.2026.65.010157

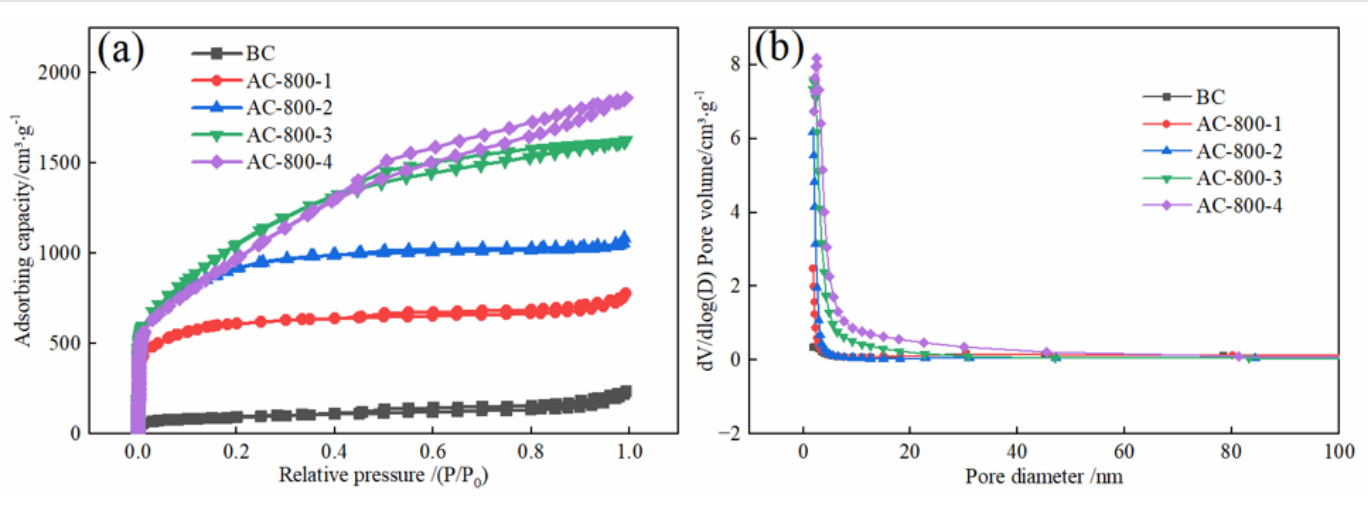

Figure 3:
a) N_2 adsorption-desorption isotherms and
b) Pore size distribution diagram of activated carbon.

This hierarchical porous structure, which is dominated by micropores and has both mesoporous and macroporous, has significant advantages: micropores contribute a high specific surface area and a large number of adsorption sites, mesopores serve as low-resistance ion transport channels, and macropores act as ion buffers, and the synergistic effect of the three jointly improves the specific capacitance and rate performance of electrode materials [13]. From the data listed in Table 3, it can be seen that with the increase of alkali-carbon ratio, the specific surface area and micropore ratio of the sample increase first and then decrease, while the average pore size gradually increases. This phenomenon can be attributed to the fact that moderate increase in alkali-carbon ratio contributes to the formation of a large number of micropores, thereby increasing the proportion of micropores and specific surface area. However, when the alkali-carbon ratio is too high, the violent activation reaction leads to the collapse of some microporous walls or the merger of adjacent micropores, transforming into mesoporous or even macroporous. Therefore, although the total pore volume continued to increase, the proportion of micropores decreased, and the mesoporous pore volume increased, and the average pore size also increased.

Scanning Electron Microscopy Analysis: The scanning electron microscope (SEM) image of BC in Figure 4(a) shows an overall smooth and dense surface, with only a few sparse pores, a morphological feature consistent with its relatively low specific surface area (357.97 m^2/g), indicating that the high-temperature carbonization process alone contributes little to the pore structure. After KOH activation, the surface morphology of the material changes significantly. AC-800-1 and AC-800-2 (Figures 4b & 4c) exhibit rich and well-developed porous structures, forming a continuous porous network. This morphological difference is consistent with the significant differences in specific surface area and total pore volume between BC and the two activated carbons shown in Table 3. This significant change mainly originates from the strong chemical etching effect on the carbon framework during the KOH activation process. This reaction creates a large number of pores, which not only significantly increases the specific surface area but also provides more active sites for ion adsorption. With the further increase of the alkali-to-carbon ratio, the surface of AC-800-3 (Figure 4d) exhibits an open pore structure with significantly enlarged pore sizes, an increased number of pores, and interconnectivity, indicating that the intense chemical corrosion at a high alkali-to-carbon ratio leads to the merging of some micropores to form mesopores and a small number of macropores.

This observation strongly corresponds with the significant decrease in micropore ratio of AC-800-3 shown in Table 3. In AC-800-4 (Figure 4e), the morphology further evolves into a continuous network structure composed of super-large pores intertwined with fine internal pores, with some pore walls showing signs of breakage and reorganization. This morphological feature indicates that its pore system is more open and has stronger connectivity. The evolution pattern of pore structures observed by SEM (micropore formation → micropore merging to form mesopores/ macropores → excessive pore expansion) is highly consistent with the pore structure parameters in Table 3 (such as increased average pore size and decreased micropore proportion), indicating that KOH activation can effectively generate abundant micropores through carbon etching, significantly enhancing the specific surface area and the number of adsorption sites; under higher alkali-to-carbon ratio conditions, it further induces micropore merging to form mesopores and macropores, thereby broadening ion transport pathways and reducing diffusion resistance. This controllable hierarchical pore system synergistically provides a structural basis for improving the electrochemical performance of electrode materials.

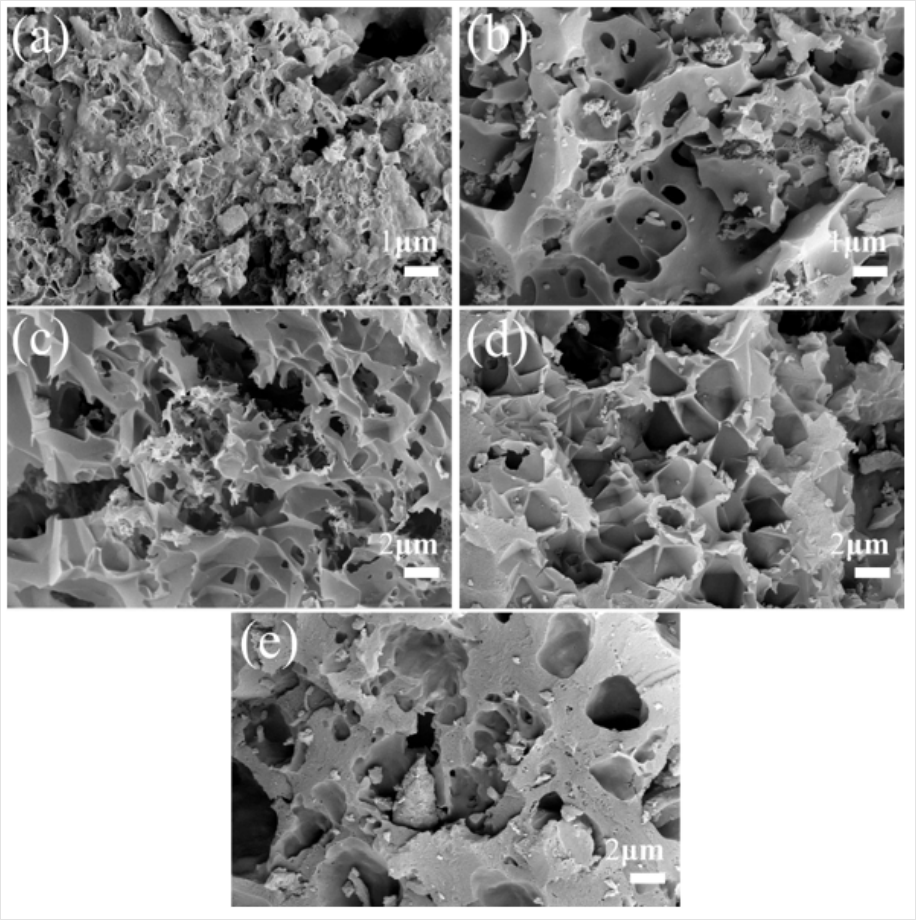

Figure 4: SEM image of activated carbon:
a) BC,
b) AC-800-1,
c) AC-800-2,
d) AC-800-3,
e) AC-800-4.

Electrochemical Performance Testing

To systematically evaluate the electrochemical performance of activated carbon samples, tests were conducted using a three-electrode system in 6 M KOH electrolyte. As shown in Figure 5(a), the CV curves of all samples at different scan rates exhibit an almost rectangular shape, indicating their typical double-layer capacitance behavior, with good reversibility and reaction stability [14]. Among them, the CV curve of AC-800-3 encloses the largest area, indicating its superior capacitance performance, which is closely related to its higher specific surface area and well-developed microporous structure, providing abundant active sites for ion migration and adsorption [15]. GCD test results (Figure 5b) further confirmed the capacitive behavior of the material. All curves exhibited highly symmetrical triangular shapes, with no significant voltage drop, reflecting low internal resistance and good reversibility. AC-800-3 showed the longest charge-discharge time, corresponding to the highest specific capacitance. According to formula (2), at a current density of 0.5 A/g, the specific capacitances of BC, AC-800-1, AC-800-2, AC-800-3, and AC-800-4 were 155.44 F/g, 195.02 F/g, 255.06 F/g, 326.03 F/g, and 301.47 F/g, respectively.

The slight distortion of the GCD curves at high potential regions is also consistent with pseudocapacitive behavior. With increasing scan rate and current density, the CV curves of AC-800-3 still maintained a good rectangular shape (Figure 5c), and the GCD curves showed no obvious deformation (Figure 5d), indicating excellent rate performance. This phenomenon can be attributed to its hierarchical pore structure: micropores (providing a specific surface area up to 3096.3 m^2/g) contribute a large number of adsorption sites, while mesopores/macropores provide efficient pathways for rapid ion diffusion, jointly optimizing charge storage and transport kinetics. As shown in Figure 5(e), AC-800-3 exhibited the highest specific capacitance in the

DOI: 10.26717/BJSTR.2026.65.010157

range of 0.5–10 A/g, and maintained a capacity of 75.22% at a high current density of 10 A/g, showing excellent rate performance. The dynamic properties of the electrode process were further explored by EIS analysis (Figure 5f). The intercept between the high-frequency curve and the real axis represents the equivalent series resistance Rs [16], and the Rs values are sorted from largest to smallest: AC-800-2 > AC-800-4 > BC > AC-800-1 > AC-800-3, where AC-800-3 has the lowest Rs (0.56 Ω), indicating that it has the best electronic conductivity.

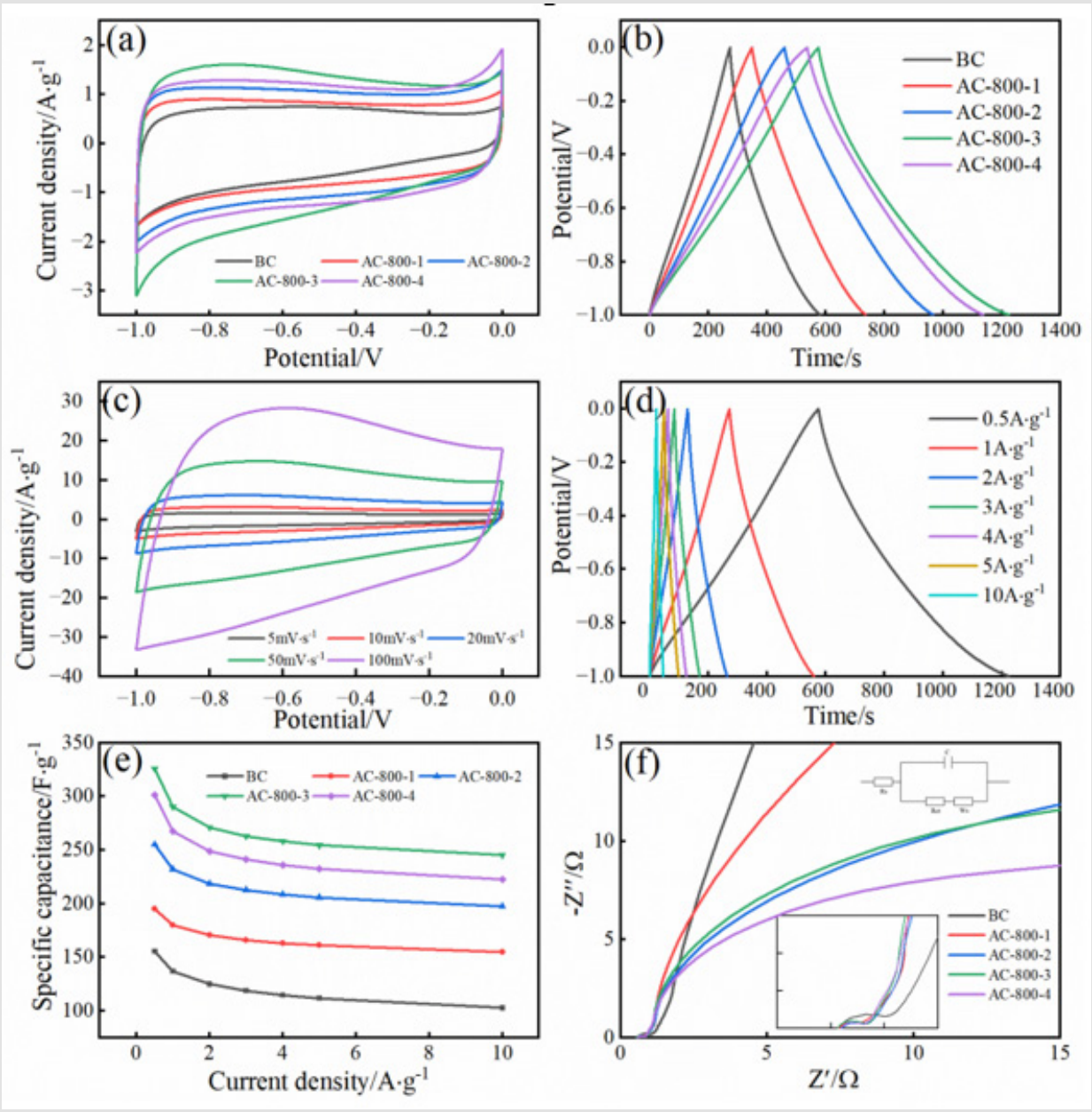

Figure 5:

a) CV curve at a scanning rate of 5mV/s;
b) GCD curve at an current density of 0.5A/g;
c) CV curves of AC-800-3 at different scanning rates;
d) GCD curves of AC-800-3 at different current densities;
e) Specific capacitance at different current densities;
f) Electrochemical impedance spectroscopy.

The diameter of the semicircle in the mid-frequency region represents the charge transfer resistance Rct [15], and the Rct of AC-800-3 and AC-800-4 is the smallest. All samples have near-vertical curves in the low frequency region, indicating ideal capacitance characteristics, with AC-800-3 having the largest slope and representing a faster ion diffusion rate. Comparing the specific capacitance value of AC-800-3 with the waste biomass-derived activated carbon in the existing literature (Table 4), it can be seen that the residue-based activated carbon prepared in this study has obvious advantages in specific capacitance and shows good application potential. To further evaluate the performance of activated carbon samples in practical supercapacitors, symmetric supercapacitors were assembled using 6 M KOH aqueous solution as the electrolyte, and their electrochemical properties were systematically tested (Figure 6). As shown in Figures 6(a) & (b), all samples exhibited typical electric double-layer capacitance behaviour, with the supercapacitor assembled from AC-800-3 showing the largest CV curve integration area and the longest GCD charge-discharge time, indicating that it possesses the highest charge storage capacity.

Table 4: Comparison of specific capacitance between biomass-derived activated carbon and AC-800-3.

Carbon Precursor	Activator	Specific Capacitance (F/g)	Electrolyte	Current Density	Reference
Waste Rice Husk	KOH	147F/g	6 M KOH	0.1A/g	[25]
Waste Bamboo	KOH	258 F/g	6 M KOH	0.1A/g	[26]
Pea Pod	KOH	192.7 F/g	6 M KOH	1mA/cm^2	[27]
Lotus Seedpod Shell	KOH	165 F/g	3 M KOH	0.5A/g	[28]
Banana Tissues	KOH, $ZnCl_2$	66 F/g	1 M Na_2SO_4	0.5 A/g	[29]
Pinus Roxburghii	KOH	78 F/g	1 M Na_2SO_4	1 A/g	[30]
Purple Corncob	KOH	195 F/g	1 M H_2SO_4	0.5A/g	[31]
Chemical Medicine Residue	KOH	326.03 F/g	6 M KOH	0.5 A/g	This work

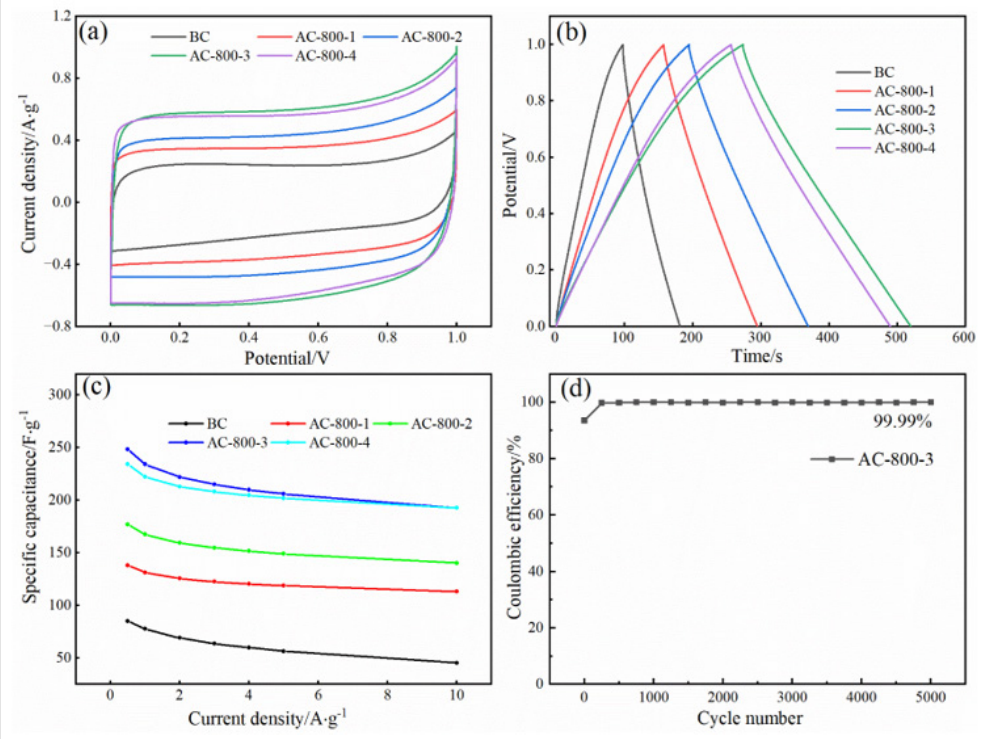

Figure 6:

a) CV curves at a scan rate of 5 mV/s;

b) GCD curves at a current density of 0.5 A/g;

c) Specific capacitance at different current densities;

d) 5000 cycles of the AC-800-3 symmetric capacitor at a current density of 1 A/g.

According to Equation (1), at a current density of 0.5 A/g, the specific capacitance based on the total mass of electrode materials was calculated to be: BC (85.21 F/g), AC-800-1 (138.15 F/g), AC-800-2 (176.85 F/g), AC-800-3 (248.6 F/g), AC-800-4 (234.34 F/g). The excellent capacitive performance of AC-800-3 is mainly attributed to its optimized hierarchical pore structure, which not only provides abundant ion adsorption sites but also ensures efficient transport of electrolyte ions. Figure 6(c) shows the rate performance of the capacitor at current densities ranging from 0.5 to 10 A/g. AC-800-3 consistently exhibits the highest specific capacitance, and even at a high current density of 10 A/g, its specific capacitance still retains 77.51% of the capacity at 0.5 A/g, demonstrating excellent rate performance. This result is closely related to its well-developed porous structure, which effectively facilitates rapid ion transport at high currents and mitigates diffusion limitations. In addition, the symmetric capacitor assembled with AC-800-3 maintains a Coulombic efficiency of approximately 99.99% after 5,000 cycles at a current density of 1 A/g (Figure 6d), fully demonstrating the capacitor's outstanding electrochemical cycling stability.

Using 1 M Et_4NBF_4/PC as the electrolyte, a symmetric AC-800-3 capacitor was assembled in a super-purified glove box, and its electrochemical performance was tested at a high operating voltage of 0-2.5 V. The results are shown in Figure 7. The cyclic voltammetry and galvanostatic charge-discharge curves in Figures 7(a) & (b) maintain good rectangular and symmetric triangular shapes, respectively, and even at higher scan rates and current densities, no significant distortion is observed, indicating that the capacitor still exhibits excellent capacitance behaviour and electrochemical reversibility in organic electrolytes [17]. As shown in Figure 7(c), the specific capacitance of the AC-800-3 symmetric capacitor decreases only slightly as the current density increases, with a specific capacitance of 225.75 F/g at 0.5 A/g and still maintaining 214.03 F/g at 10 A/g, resulting in a capacitance retention rate as high as 94.8%, demonstrating excellent rate performance. Figure 7(d) shows the relationship between the device's energy density and power density. According to calculations using formulas (3) and (4), the energy density reaches 45.3 Wh/kg at a power density of 309.23 W/kg; even when the power density increases to 4988.5 W/kg, the energy density can still be maintained at 26.74 Wh/kg. Compared with other biomass-based carbon materials [18-24], this device shows a significant advantage in terms of both energy and power characteristics [25-31].

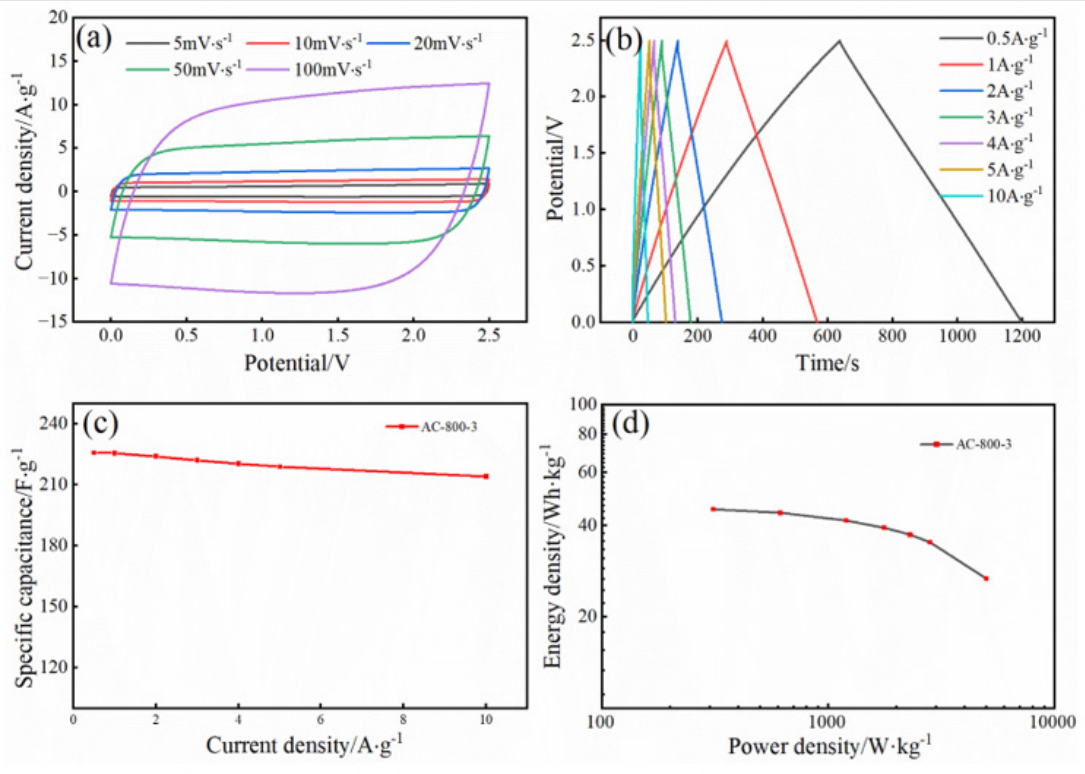

Figure 7:

a) CV curves of the AC-800-3 symmetric capacitor at different scan rates;
b) GCD curves at different current densities;
c) Specific capacitance at different current densities;
d) Ragone plot (energy density vs. power density.

Conclusions

This study successfully transformed hazardous waste pharmaceutical residues into high-performance porous carbon materials through a pre-carbonization–deashing–KOH activation process, systematically revealing the regulatory mechanism of the alkali-to-carbon ratio on the material's structure and electrochemical performance. As the alkali-to-carbon ratio increases, the degree of graphitization of the material decreases, defect density significantly increases, and the pore structure is effectively optimized; however, an excessively high alkali-to-carbon ratio can also cause partial collapse of the microporous structure, leading to an increase in the proportion of mesopores and macropores. Electrochemical test results indicate that the prepared Western medicine residue-based capacitive carbon exhibits excellent specific capacitance and rate performance in a three-electrode system, outperforming most reported biomass carbon materials. This is mainly attributed to its high specific surface area, hierarchical porous structure, and possibly existing surface functional groups.

The further assembled symmetric supercapacitors demonstrate high specific capacitance, excellent cycling stability, and high energy density in both aqueous and organic electrolytes, showing good potential for practical applications. This study achieved a high-value conversion of hazardous pharmaceutical waste residue into high-performance capacitive carbon by constructing a hierarchical porous structure through adjusting the alkali-to-carbon ratio and optimizing electrochemical performance. It exhibited excellent comprehensive performance in various electrolyte systems. This provides a feasible technical pathway for the resource utilization and high-value application of pharmaceutical solid waste, and has important reference value for the development of green and economical biomass-based energy storage materials.

References

1. Han J, Lee J H, Roh K C (2018) Herbaceous Biomass Waste-Derived Activated Carbons for Supercapacitors. Journal of Electrochemical Science and Technology 9(2): 157-162.
2. Du W, Wang X, Sun X, Jie Zhan, Huadong Zhang, et al. (2018) Nitrogen-doped hierarchical porous carbon using biomass-derived activated carbon/carbonized polyaniline composites for supercapacitor electrodes. Journal of Electroanalytical Chemistry 827: 213-220.
3. Chaiammart N, Vignesh V, Thu M M, Apiluck Eiadua, Thandavarayan Maiyalagan, et al. (2024) Chemically activated carbons derived from cashew nut shells as potential electrode materials for electrochemical supercapacitors. Carbon Resources Conversion 8(2): 100267.
4. Han F, Li S, Jing P, Yanhui Li, Mingcheng Chang, et al. (2025) Sargassum/chitin-derived nitrogen-doped activated carbon with exceptional electrochemical performance for supercapacitors. International Journal of Electrochemical Science 20(6): 101024.
5. Xie L, Sun G, Su F, Xiaoqian Guo, Qingqiang Kong, et al. (2016) Hierarchical porous carbon microtubes derived from willow catkins for supercapacitor applications. Journal of Materials Chemistry A 4(5): 1637-1646.
6. Sandhiya M, Nadira M P, Sathish M (2021) Fabrication of Flexible Supercapacitor Using N-Doped Porous Activated Carbon Derived from Poultry Waste. Energy & Fuels 35(18): 15094-15100.
7. Rawal S, Joshi B, Kumar Y (2018) Synthesis and characterization of activated carbon from the biomass of Saccharum bengalense for electrochemical supercapacitors. Journal of Energy Storage 20: 418-426.
8. Ferrari A, Robertson J (2000) Interpretation of Raman spectra of disordered and amorphous carbon. Physical Review B 61(20): 14095-14107.
9. Kumbhar D, Palliyarayil A, Reghu D, D Shrungar, S Umapathy, et al. (2021) Rapid discrimination of porous bio-carbon derived from nitrogen rich biomass using Raman spectroscopy and artificial intelligence methods. Carbon 178: 792-802.
10. Liu X, Choi J, Xu Z, Clare Grey, Simon Fleischmann, et al. (2024) Raman Spectroscopy Measurements Support Disorder-Driven Capacitance in Nanoporous Carbons. Journal of the American Chemical Society 146(45): 30752.
11. Thommes M, Kaneko K, Neimark A V, James P Olivier, Francisco Rodriguez Reinoso, et al. (2015) Physisorption of gases, with special reference to the evaluation of surface area and pore size distribution (IUPAC Technical Report). 87(9-10): 1051-1069.
12. Gao Y, Zhang W, Yue Q, Baoyu Gao, Yuanyuan Sun, et al. (2014) Simple synthesis of hierarchical porous carbon from Enteromorpha prolifera by a self-template method for supercapacitor electrodes. Journal of Power Sources 270: 403-410.
13. Zheng X, Luo J, Lv W, Da Wei Wang, Quan Hong Yang (2015) Two-Dimensional Porous Carbon: Synthesis and Ion-Transport Properties. Advanced Materials 27(36): 5388-5395.
14. Song X, Ma X, Li Y, Liang Ding, Ruiyu Jiang (2019) Tea waste derived microporous active carbon with enhanced double-layer supercapacitor behaviors. Applied Surface Science 487: 189-197.
15. Wang K, Zhang Z, Sun Q, Peng Wang, Yueming Li (2020) Durian shell-derived N, O, P-doped activated porous carbon materials and their electrochemical performance in supercapacitor. Journal of Materials Science 55: 10142-10154.
16. Wang C, Wu D, Wang H, Zhiyong Gao, Fang Xu, et al. (2018) Biomass derived nitrogen-doped hierarchical porous carbon sheets for supercapacitors with high performance. Journal of Colloid and Interface Science 523: 133-143.
17. Xiaoyun Z, Bingkang S, Xing F, Peng Liang, Guoming Zhao, et al. (2021) Hierarchical porous carbon derived from coal and biomass for high performance supercapacitors. Fuel 311: 122552.
18. Zhang J, Gong X, Li X, Fanda Zeng, Zeyu Hao, et al. (2023) Electron-ion conjugation sites co-constructed by defects and heteroatoms assisted carbon electrodes for high-performance aqueous energy storage. Journal of Colloid and Interface Science 640: 600-609.
19. Quan H, Tao W, Wang Y, Dezhi Chen (2022) Enhanced supercapacitor performance of Camellia oleifera shell derived hierarchical porous carbon by carbon quantum dots. Journal of Energy Storage 55: 105573.
20. Dhakal G, Kumar D R, Sahoo S, Jae Jin Shim (2023) Litchi seed biowaste-derived activated carbon supporting matrix for efficient symmetric and asymmetric supercapacitors. Carbon 208: 277-289.
21. Li L, Zhou Y, Zhou H, Haonan Qu, Chengli Zhang, et al. (2019) N/P Codoped Porous Carbon/One-Dimensional Hollow Tubular Carbon Heterojunction from Biomass Inherent Structure for Supercapacitors. ACS Sustainable Chemistry & Engineering 7(1): 1337-1346.
22. Deng J, Xiong T, Xu F, Mingming Li, Chuanlong Han, et al. (2015) Inspired by Bread Leavening: One-pot Synthesis of Hierarchically Porous Carbon for Supercapacitors. Green Chemistry 17(7): 4053-4060.
23. Zhu G, Ma L, Lv H, Yi Hu, Tao Chen, et al. (2016) Pine needle-derived microporous nitrogen-doped carbon frameworks exhibit high performances

in electrocatalytic hydrogen evolution reaction and supercapacitors. Nanoscale 9(3): 1237-1243.

24. Du J, Liu L, Hu Z, Yifeng Yu, Yue Zhang, et al. (2018) Raw-Cotton-Derived N-Doped Carbon Fiber Aerogel as an Efficient Electrode for Electrochemical Capacitors. ACS Sustainable Chemistry & Engineering 6(3): 4008-4015.
25. Liu D, Zhang W, Lin H, Yang Li, Haiyan Lu, et al. (2016) A green technology for the preparation of high capacitance rice husk-based activated carbon. Journal of Cleaner Production 112: 1190-1198.
26. Yang C S, Jang Y S, Jeong H K (2014) Bamboo-based activated carbon for supercapacitor applications. Current Applied Physics 14(12): 1616-1620.
27. Ahmed S, Ahmed A, Rafat M (2018) Impact of aqueous and organic electrolytes on the supercapacitive performance of activated carbon derived from pea skin. Surface & Coatings Technology 349: 242-250.
28. Sekar M, Sakthi V, Rengaraj S (2004) Kinetics and equilibrium adsorption study of lead (II) onto activated carbon prepared from coconut shell. Journal of Colloid and Interface Science 279(2): 307-313.
29. Subramanian V, Luo C, Stephan A M, Kee Suk Nahm, Sabu Thomas, et al. (2007) Supercapacitors from Activated Carbon Derived from Banana Fibers. The Journal of Physical Chemistry C 111(20): 7527-7531.
30. Manyala N, Bello A, Barzegar F, A A Khaleed, D Y Momodu, et al. (2016) Coniferous pine biomass: A novel insight into sustainable carbon materials for supercapacitors electrode. Materials Chemistry and Physics 182: 139-147.
31. Huarote Garcia E, Cardenas Riojas A A, Monje I E, Elvis O Lopez, Ofelia M Arias Pinedo, et al. (2024) Activated Carbon Electrodes for Supercapacitors from Purple Corncob (Zea mays L.). ACS Environmental Au 4(2): 80-88.

ISSN: 2574-1241

DOI: 10.26717/BJSTR.2026.65.010157

Muhammad Abdullah Ismail. Biomed J Sci & Tech Res

Submission Link: https://biomedres.us/submit-manuscript.php